

Origin of the significantly enhanced optical transitions in layered boron nitride

Bing Huang,¹ X. K. Cao,² H. X. Jiang,² J. Y. Lin,² and Su-Huai Wei¹

¹National Renewable Energy Laboratory, 1617 Cole Boulevard, Golden, Colorado 80401, USA

²Department of Electrical and Computer Engineering, Texas Tech University, Lubbock, Texas 79409, USA

(Received 24 February 2012; revised manuscript received 24 April 2012; published 1 October 2012)

It is normally expected that an excellent optical material should have $p \rightarrow s$ -like transitions at the absorption edge. This is because the strength of $p \rightarrow s$ -like transitions usually is much stronger than those of $p \rightarrow p$ transitions, especially in those ionic semiconductors where the electronic states are more localized and behave as atomic characters. Here, we demonstrate an exception that the luminescence intensity of hexagonal boron nitride (h -BN) could be at least two orders of magnitude greater than that of AlN, despite the dominated atomic $p \rightarrow p$ transitions at the absorption edge of h -BN. Using group theory analysis and first-principles calculations, we show that the strong optical transitions in h -BN originate from the unusually strong $p \rightarrow p$ -like transitions and its “two-dimensional” nature. As learned from h -BN, we demonstrate that one can dramatically increase the absorption or luminescence intensity at the fundamental absorption edge of an optical material by confining its thickness into a few layers, which is much more effective than the commonly used superlattice technology.

DOI: [10.1103/PhysRevB.86.155202](https://doi.org/10.1103/PhysRevB.86.155202)

PACS number(s): 78.66.-w, 71.15.Mb, 71.20.Nr, 78.20.-e

I. INTRODUCTION

The optical absorption coefficient $\alpha(\omega)$ and photoluminescent intensity $I(\omega)$ are mostly determined by the quantum transition rate $W_{i \rightarrow f}$ given by Fermi's golden rule $W_{i \rightarrow f} \propto |M|^2 g(\hbar\omega)$, where $|M|^2 = |\langle f | \vec{e} \cdot \vec{p} | i \rangle|^2$ is the dipole matrix element square between states i and f , and $g(\hbar\omega)$ is the joint density of states^{1,2} with $\hbar\omega = E_f - E_i$ where E_f and E_i are the energy of states f and i . In the textbook description, one learns that, in a spherically symmetric atom, an allowed optical electric-dipole transition requires that the orbital angular momentum l of the initial and final states differ by ± 1 , i.e., atomic $p \rightarrow p$ transition is forbidden, but the $p \rightarrow s$ transition is expected to have large magnitude. When atoms form a crystal, due to reduced symmetry, even though this kind of $p \rightarrow p$ transition may not be completely forbidden, it is normally expected that the crystal inherits the atomic features; thus the strengths of $p \rightarrow p$ -like transitions should be much weaker than those of $p \rightarrow s$ transitions, especially in those ionic semiconductors where the electronic states are more localized and behave as atomic characters. Until now, the preferred optical materials have been mostly those semiconductors with $p \rightarrow s$ transitions at the absorption edges. For example, group-III nitrides AlN, GaN, InN, and their alloys are widely used in solid-state lighting for ultraviolet (UV) and visible lights.³

AlN and its related materials play a dominant role in deep-UV applications due to their suitable band gaps and strong optical transition rates at the absorption edge.³ Layered hexagonal BN (h -BN), although it has a band gap close to that of AlN, was initially not considered a good optical material because, as in most layered ionic semiconductors, its conduction and valence band edges both have atomic p_z characters. Therefore, it is quite unexpected that experimentally it has been shown that h -BN can exhibit high light-emitting intensity for deep-UV lasing and LED applications.⁴ To develop future optical materials, it will be quite important to understand the fundamental origin of why h -BN could be a good emitter and what are the advantages of layered h -BN compared to other conventional high-efficiency optical materials such as AlN.

By employing experimental measurements and first-principles calculations, we demonstrate that atomic-like $p \rightarrow p$ transitions are not only allowed in h -BN due to reduced symmetry, but can also have very large transition rates due to the small B-N bond length, and thus large overlap between B and N p orbitals. The unusual $p \rightarrow p$ transitions combined with the large joint density of states of electron-hole pairs resulting from the “two-dimensional” nature of h -BN lead to a high absorption or luminescence intensity at the fundamental absorption edge, which is at least two orders of magnitude greater than that of AlN. As learned from h -BN, we demonstrate that the absorption or luminescence intensity at the fundamental absorption edge of an optical material can be largely enhanced by confining its thickness into a few layers.

II. EXPERIMENTAL AND COMPUTATIONAL METHODS

AlN epilayers are grown at 1200 °C using hydrogen as a carrier gas with a growth rate of about 1 $\mu\text{m}/\text{h}$. Epitaxial layers of h -BN are produced using triethylboron (TEB) and ammonia (NH_3) as B and N sources, respectively. A thin BN buffer layer is deposited at 650 °C prior to the growth of the epilayer. h -BN epilayers are grown at 1300 °C using hydrogen as a carrier gas with a growth rate of 0.5 $\mu\text{m}/\text{h}$. X-ray diffraction (XRD) measurements reveal that AlN and h -BN samples employed in this work have a full width at half maximum (FWHM) of ~ 400 arc sec for a (002) rocking curve. Photoluminescence (PL) signals are collected in two different configurations of the polarization of emitted light, e.g., the electrical field of the PL emission is directed either parallel ($\vec{e} \parallel \vec{c}$) or perpendicular ($\vec{e} \perp \vec{c}$) to the c axis. The PL spectra of h -BN and AlN are measured with identical conditions with two samples sitting side by side vertically, and PL data are collected for each by moving the samples through the use of a vertical translational stage. A frequency-quadrupled Ti-sapphire laser with a repetition rate of 76 MHz and 100 fs pulse width operating at 197 nm is focused onto the sample surface through a microscope objective. The collected PL signal is then dispersed by a 1.3 m monochromator and detected by a micro-channel-plate photomultiplier tube.

All the density-functional-theory (DFT) calculations are performed by using the VASP code.⁵ Projector augmented wave (PAW) potentials are used to describe the interaction of core and valence electrons, and a generalized gradient approximation (GGA) with the PBE functional is selected in our calculations. It is well known that GGA type calculations usually underestimate the band gaps of semiconductors, and hybrid functional calculations could give improved results for both conventional semiconductors, thus we adopt a hybrid functional⁶ to calculate the electronic structures. A 20 Å vacuum region is included when we calculate the nanostructures. The pseudo-H method⁷ is used to passivate the surfaces of BN quantum dot (QD), AlN thin film, and GaN thin film. Enough k -point sampling is used for the Brillouin-zone integration. The energy cutoff is set to 500 eV and structural optimization is carried out on all systems until the residual forces converge to 0.01 eV/Å. The detailed methods of optical calculations are described in Ref. 8. The symmetry related calculations and analysis are done in QUANTUM ESPRESSO code.⁹ Moreover, the GW correction and Bethe-Salpeter equation calculations are carried out in YAMBO project code.¹⁰ For the calculations performed with the YAMBO code, the ground-state Kohn-Sham wave functions and eigenvalues are obtained using a local-density approximation (LDA) exchange-correlation functional with Troullier-Martins norm-conserving pseudopotentials, as implemented in QUANTUM ESPRESSO code. A kinetic energy cutoff of 100 Ry is used for the wave function. These calculations are carried out to obtain an input compatible with the YAMBO code.

III. RESULTS AND DISCUSSION

Epitaxial AlN and h -BN with thicknesses of $\sim 1.0 \mu\text{m}$ are synthesized by metal-organic chemical-vapor deposition on (0001) sapphire substrates. The PL spectra of h -BN and AlN are measured with identical conditions with two samples sitting side by side vertically, and PL data are collected for each by moving the samples through the use of a vertical translational stage. As shown in Fig. 1, the PL measurements show that the peak intensity of h -BN along $\vec{e} \perp \vec{c}$ is about twice as large as $\vec{e} \parallel \vec{c}$. In contrast to h -BN, the emission along $\vec{e} \perp \vec{c}$ in AlN is almost forbidden (a very small angle in collection configuration makes the recorded I_{emi} of AlN nonzero along $\vec{e} \perp \vec{c}$). Surprisingly, we find that the emission from h -BN is at least 400 times greater (peak intensity) than that of AlN from the allowed transitions. This is unusual because the strength of the $p \rightarrow s$ transition at the AlN absorption edge is expected to be much stronger than that of the atomic-like $p \rightarrow p$ transition in h -BN. Therefore, an interesting question is why strong optical transition rates can exist in h -BN.

In order to investigate the strong optical transitions in h -BN, we have studied the possibility and strengths of $p \rightarrow p$ transitions in BN structures. BN is known to have three different crystal structures: cubic zinc-blende BN (c -BN), hexagonal wurzite BN (w -BN), and h -BN.¹¹ We first examine the probability of $p \rightarrow p$ transitions in these BN structures by using the general group theory analysis, and then we calculate the size of $|M|^2$ for the $p \rightarrow p$ transitions. In the following, we will focus on the electron-dipole transitions at the Γ point where the symmetry is the same as that of the crystal.

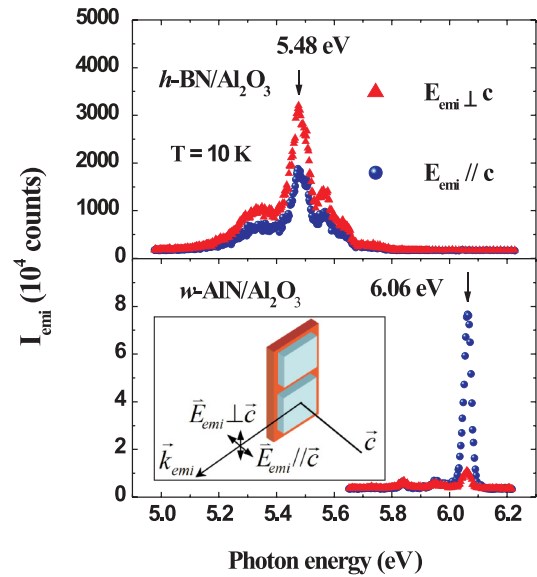


FIG. 1. (Color online) The PL emission spectra of h -BN and w -AlN epilayers grown on sapphire substrate by metal-organic chemical-vapor deposition, which is collected in the configuration of the electrical field of emission perpendicular ($\vec{E} \perp \vec{c}$) and parallel ($\vec{E} \parallel \vec{c}$) to the c axis, respectively, controlled through the use of a polarizer in front of the monochromator.

In a zinc-blende crystal (T_d symmetry), \vec{P} belongs to a Γ_{15} ^{12,13} irreducible representation and the matrix element is isotropic. Our calculations show that for sp semiconductors the representations of the four valence bands are Γ_1 and Γ_{15} , with Γ_{15} as the valence-band maximum. The wave functions generated from the operation of \vec{P} on Γ_{15} states can be reduced to a direct sum of irreducible representations, i.e., $\vec{P}|\Gamma_{15}\rangle = \Gamma_1 \oplus \Gamma_{12} \oplus \Gamma_{15} \oplus \Gamma_{25}$. In terms of the matrix-element theory, this indicates that dipole transitions from a Γ_{15} valence band are only allowed to conduction bands with Γ_1 , Γ_{12} , Γ_{15} , or Γ_{25} symmetries (Table I). Thus, like the $p \rightarrow s$ ($\Gamma_{15} \rightarrow \Gamma_1$) transition, the $p \rightarrow p$ ($\Gamma_{15} \rightarrow \Gamma_{15}$) transition is also allowed. Our calculations show that, surprisingly, the strength of the $p \rightarrow p$ ($|\langle \Gamma_{15} | \vec{e} \cdot \vec{P} | \Gamma_{15} \rangle|^2 = 1.13$) transition is comparable to that of the $p \rightarrow s$ ($|\langle \Gamma_1 | \vec{e} \cdot \vec{P} | \Gamma_{15} \rangle|^2 = 1.24$)

TABLE I. Symmetry analysis of the representations of the momentum operator, the top of the valence band wave functions, and the direct product $\vec{P}|v\rangle$ at the Γ point, which determines the conduction band states that can have allowed dipole transition for T_d , C_{6v} , and D_{6h} symmetries.

| Symmetry | \vec{P} | $ v\rangle$ | $\vec{P} v\rangle$ |
|----------|--|---------------|---|
| T_d | Γ_{15} | Γ_{15} | $\Gamma_1 \oplus \Gamma_{12} \oplus \Gamma_{15} \oplus \Gamma_{25}$ |
| C_{6v} | Γ_6 ($\vec{e} \perp \vec{c}$) | Γ_6 | $\Gamma_1 \oplus \Gamma_2 \oplus \Gamma_3$ |
| | Γ_1 ($\vec{e} \parallel \vec{c}$) | Γ_6 | Γ_6 |
| | Γ_6 ($\vec{e} \perp \vec{c}$) | Γ_1 | Γ_6 |
| | Γ_1 ($\vec{e} \parallel \vec{c}$) | Γ_1 | Γ_1 |
| D_{6h} | Γ_6^- ($\vec{e} \perp \vec{c}$) | Γ_6^- | $\Gamma_1^+ \oplus \Gamma_2^+ \oplus \Gamma_5^+$ |
| | Γ_2^- ($\vec{e} \parallel \vec{c}$) | Γ_6^- | Γ_6^+ |
| | Γ_6^- ($\vec{e} \perp \vec{c}$) | Γ_2^- | Γ_6^+ |
| | Γ_2^- ($\vec{e} \parallel \vec{c}$) | Γ_2^- | Γ_1^+ |

transition. It is also surprising to note that the strengths of $p \rightarrow p$ transitions in c -BN are two times larger than those in silicon. Further investigation shows that, although the $p \rightarrow p$ within the same atom is weak, the $p \rightarrow p$ transition between different atoms is allowed and can be large if the atomic wave-function overlap between neighboring atoms is large. Because the bond length of B-N (1.55 Å) is much shorter than that of Si-Si (2.34 Å), this explains why c -BN can have much stronger $p \rightarrow p$ transitions than silicon.

For a wurzite crystal structure with C_{6v} symmetry, the transition is anisotropic with respect to the c axis, which induces a crystal field that splits the top of the valence band from the Γ_{15} symmetry into a twofold degenerate Γ_6 state and nondegenerate Γ_1 state.^{14–16} Closer examination shows that P_x and P_y transform as the rows of Γ_6 , while P_z transforms as Γ_1 .¹⁷ As shown in Table I, the strengths of the $p \rightarrow p$ transitions are sensitive to the polarization of light \vec{e} . For example, the $\Gamma_6 \rightarrow \Gamma_6^*$ transition is forbidden if $\vec{e} \perp \vec{c}$, but allowed when $\vec{e} \parallel \vec{c}$ (the calculated $|\langle \Gamma_6 | P_{\parallel} | \Gamma_6 \rangle|^2 = 0.94$ for w -BN). Similarly, the $\Gamma_1 \rightarrow \Gamma_1^*$ transition is allowed (the calculated $|\langle \Gamma_1 | P_{\parallel} | \Gamma_1 \rangle|^2 = 1.82$ for w -BN) only if $\vec{e} \parallel \vec{c}$. Generally, the strengths of the $\Gamma_6 \rightarrow \Gamma_6^*$ and $\Gamma_1 \rightarrow \Gamma_1^*$ transitions are larger than those of the $\Gamma_1 \rightarrow \Gamma_6^*$ and $\Gamma_6 \rightarrow \Gamma_1^*$ transitions (e.g., $|\langle \Gamma_6 | P_{\perp} | \Gamma_1 \rangle|^2 = 0.52$) due to the larger (smaller) overlap of the wave functions between the N $p_{x,y}$ (p_z) and B $p_{x,y}$ (p_z) orbitals.

The situation of the layered hexagonal structure (D_{6h} symmetry) is similar to that of the wurzite structure except that it also has inverse symmetry. Therefore, $\vec{e} \cdot \vec{P}$ transforms as Γ_6^- if $\vec{e} \perp \vec{c}$, but as Γ_2^- if $\vec{e} \parallel \vec{c}$,¹⁸ as shown in Table I. Due to the inverse symmetry, only even (+ parity) to odd (– parity) or odd to even transitions are allowed. Under D_{6h} symmetry, only the $\sigma \rightarrow \sigma^*$ ($|\langle \Gamma_5^+ | P_{\perp} | \Gamma_6^- \rangle|^2 = 2.85$) transition is allowed when $\vec{e} \perp \vec{c}$ (Table I), while $\pi \rightarrow \pi^*$ ($\Gamma_2^- \rightarrow \Gamma_3^+$) and $\sigma(\pi) \rightarrow \pi^*(\sigma^*)$ [e.g., $\Gamma_6^- (\Gamma_2^-) \rightarrow \Gamma_3^+ (\Gamma_5^+)$] transitions are forbidden independent of the polarization of the light. Compared to c -BN and w -BN, because of the ~ 0.11 Å shorter B-N bond length in h -BN and the planar structure, the wave-function overlaps between B and N atoms are stronger in h -BN; consequently, the strengths of the (allowed) $p \rightarrow p$ transitions in h -BN are significantly larger than those in c -BN and w -BN.

Although the strength of the $p \rightarrow p$ transition at the absorption edge of h -BN is comparable to that of the $p \rightarrow s$ transition at the absorption edge of AlN ($|\langle \Gamma_1 | P_{\parallel} | \Gamma_1 \rangle|^2 = 3.14$), we still cannot understand the much larger optical transition rates in h -BN. As stated earlier, besides of the strength of $|M|^2$, $W_{i \rightarrow f}$ also depends on $g(\hbar\omega)$. It is therefore interesting to know if the huge intensity of luminescence in h -BN is due to some “special” $g(\hbar\omega)$. In practice, $W_{i \rightarrow f}$ is closely related to the imaginary part of the dielectric response function $\varepsilon_i(\omega)$, which is given by $\varepsilon_i(\omega) = \frac{(8\pi)^2 e^2}{\omega^2 m^2 V} \sum_{v,c} \sum_{\vec{k}} |\langle c, \vec{k} | \vec{e} \cdot \vec{p} | v, \vec{k} \rangle|^2 \delta(E_c(\vec{k}) - E_v(\vec{k}) - \hbar\omega)$.^{1,2} Most of the dispersion of $\varepsilon_i(\omega)$, especially at the fundamental absorption edge, is determined by the summation over $\delta(E_c(\vec{k}) - E_v(\vec{k}) - \hbar\omega)$, which is equal to $g(\hbar\omega)$.^{1,2} It is known that $g(\hbar\omega)$ strongly depends on the dimensionality of a system: in a three-dimensional (3D) system, $g(\hbar\omega) \propto (E_{cv} - E_g)^{\frac{1}{2}}$; in a two-dimensional (2D) system, $g(\hbar\omega) \propto C$;

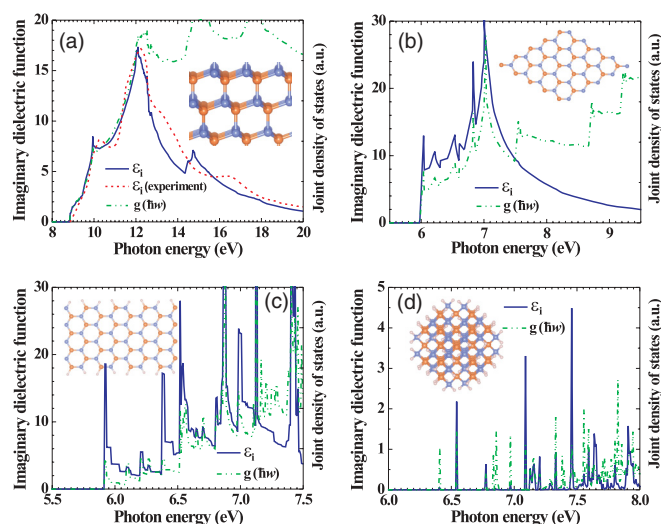


FIG. 2. (Color online) The optical property of a BN material as a function of its dimensionality. (a) 3D case: the calculated $\varepsilon_i(\omega)$ and $g(\hbar\omega)$ of c -BN. The experimental measured $\varepsilon_i(\omega)$ (Ref. 20; with blue shift) is also plotted for comparison. (b) 2D case: the calculated $\varepsilon_i(\omega)$ and $g(\hbar\omega)$ of single-layer BN. (c) 1D case: the calculated $\varepsilon_i(\omega)$ and $g(\hbar\omega)$ of a 1-nm-wide armchair-edge BNNR. (d) 0D case: the calculated $\varepsilon_i(\omega)$ and $g(\hbar\omega)$ of a BN quantum dot with a diameter around 1 nm. The corresponding structures for each case are shown as insets in each figure.

in a one-dimensional (1D) system, $g(\hbar\omega) \propto (E_{cv} - E_g)^{-\frac{1}{2}}$; and in a zero-dimensional (0D) system, $g(\hbar\omega) \propto \delta(E_{cv} - E_n)$. Compared to 3D materials, the $g(\hbar\omega)$ around E_g in a low-dimensional material is significantly enhanced as a result of the specific dispersion of $g(\hbar\omega)$ in reduced dimensionality. Consequently, it is expected that the $W_{i \rightarrow f}$ of a material at the absorption edge can be largely enhanced during the reduction of its dimensionality if $|M|^2$ is not decreased dramatically.

In order to have a clearer picture of the relationship between the optical property of a material and its dimensionality in a real material, we have calculated the $\varepsilon_i(\omega)$ and $g(\hbar\omega)$ of BN from 3D bulk to 0D quantum dot (QD), as shown in Fig. 2. c -BN is an indirect band-gap semiconductor with a minimum direct band gap around 8.8 eV at the Γ point.¹⁹ The shape of $\varepsilon_i(\omega)$ is mostly determined by $D_j(E_{cv})$, as shown in Fig. 2(a). Obviously, there is a very good overall agreement between our calculations and the experimental data²⁰ considering their shape and corresponding peaks.

When the size of BN is reduced, as we expected, the shape and intensity of $\varepsilon_i(\omega)$ and $g(\hbar\omega)$ around the absorption edge may show a significant difference. As the synthesis of 2D single-layer BN (SLBN) and 1D single-layer BN nanoribbons (BNNRs) have recently been achieved in experiments,^{21,22} they are selected as typical examples for 2D and 1D BN structures, as shown in Figs. 2(b) and 2(c). The structure of SLBN is similar to graphene but with the replacement of C by B and N, thus the π and π^* states, which have degenerate energy at the Dirac (K) point in graphene, are no longer degenerate. Our calculation shows that SLBN is semiconducting with a band gap of 5.98 eV at the K point, close to the experimental values.²¹ The fundamental absorption edge is contributed by the strong $\pi \rightarrow \pi^*$ transitions. Moreover, the 2D nature of

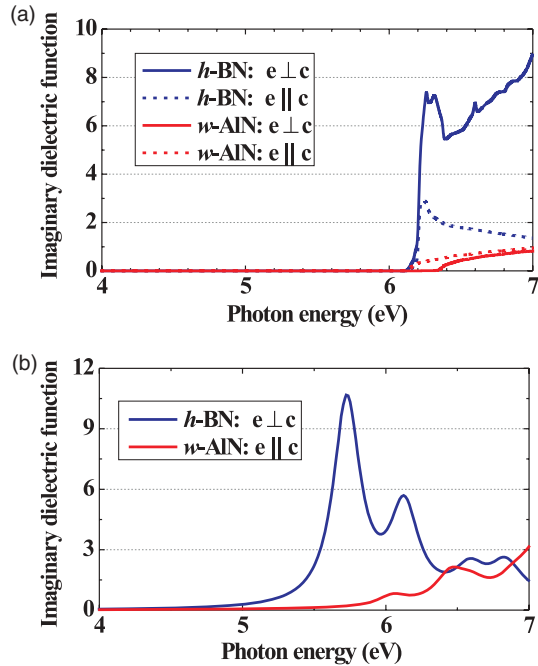


FIG. 3. (Color online) (a) The calculated $\varepsilon_i(\omega)$ of h -BN and w -AIN as a function of \vec{e} . (b) The calculated $\varepsilon_i(\omega)$ of h -BN and w -AIN obtained from the GW + BSE calculations.

SLBN induces a sharp “step”-like $g(\hbar\omega)$ around the absorption edge [Fig. 2(b)]. The strong $\pi \rightarrow \pi^*$ transitions combined with this special $g(\hbar\omega)$ give rise to high intensity of $\varepsilon_i(\omega)$ at the absorption edge.

When the dimensionality of BN is further reduced from 2D SLBN to 1D BNNRs, as shown in Fig. 2(c), the $\varepsilon_i(\omega)$ as well as the $g(\hbar\omega)$ at the absorption edge are close to the shape of $(E_{cv} - E_g)^{-\frac{1}{2}}$ and exhibit a very high intensity. Finally, a spherical c -BN QD with a diameter around 1 nm cut from the bulk is constructed [Fig. 2(d)]. As we expected, the 0D nature of the QD results in series of δ -function-like peaks in $\varepsilon_i(\omega)$. But due to the reduced strength of $|M|^2$ in BN QD, the peak intensity of $\varepsilon_i(\omega)$ at the absorption edge for BN QD is not obviously larger than that of 3D c -BN.

After knowing the relation between $\varepsilon_i(\omega)$ (or $W_{i \rightarrow f}$) and dimensionality, we now turn back to the case of h -BN. Due to the weak van de Waals interactions and large distance (3.23 Å) between each layer in h -BN, the interlayer optical transitions are much weaker than those of single-layer transitions, e.g., the strengths of the $\pi \rightarrow \pi^*$ transitions between two neighboring layers are only $\sim 20\%$ of those in the same layer. As a result, the optical properties of 3D h -BN are similar to those of 2D SLBN [Fig. 3(a)], which are mostly determined by the “2D” nature of h -BN and strong “single-layer” $p \rightarrow p$ transitions at the absorption edge. As a conventional 3D material, the dispersion of $\varepsilon_i(\omega)$ for AIN at the absorption edge is proportional to the conventional $(E_{cv} - E_g)^{\frac{1}{2}}$. The calculated $\varepsilon_i(\omega)$ of h -BN and AIN as a function of the polarization of the light \vec{e} is shown in Fig. 3(a). Compared to AIN, obviously, h -BN has a greatly enhanced absorption or luminescence intensity at the absorption edge. In h -BN, the absorption (peak) intensity along the $\vec{e} \perp \vec{c}$ direction is significantly larger than that of

$\vec{e} \parallel \vec{c}$. However, the case is opposite for AIN, where the optical transition is forbidden along $\vec{e} \perp \vec{c}$ due to the negative crystal-field splitting,^{14,15} as shown in Fig. 3(a). Our result is consistent well with the experimental observations (Fig. 1).

It is expected that the excitonic effect can be important in layered structures such as h -BN due to the enhanced electron-hole overlapping in 2D structures. In order to check our conclusion obtained from the single-particle picture, a GW plus Bethe-Salpeter equation (GW + BSE) calculation is carried out to obtain the optical spectrum of h -BN and w -AIN, including the excitonic effect. As shown in Fig. 3(b), the excitonic effects are more remarkable in h -BN than in 3D w -AIN, which shifts the transition energy of h -BN to a lower energy position, with a high-intensity peak at 5.72 eV. Compared to the minimum direct GW band gap of 6.48 eV in h -BN, the exciton binding energy is estimated to be ~ 0.76 eV, agreeing with previous calculations.²³ Obviously, this high-intensity excitonic peak is mainly contributed by the high-intensity of electron-hole pairs originating from the “2D” optical nature of h -BN, giving rise to large enhanced optical transition rate at the absorption edge compared to AIN. Thus, despite the large exciton binding energy in h -BN, results obtained from the single-particle picture are still qualitatively correct.

These findings on h -BN can inspire us to examine the approaches for optimizing the optical performance of a bulk material. As we learned from BN, the reduction of dimensionality can usually result in a large enhancement of absorption or luminescence intensity at the absorption edge, if $|M|^2$ is not decreased dramatically. If one can reduce a bulk material to a 2D slab with a certain thickness that is comparable to the magnitude of the radius of a free exciton,

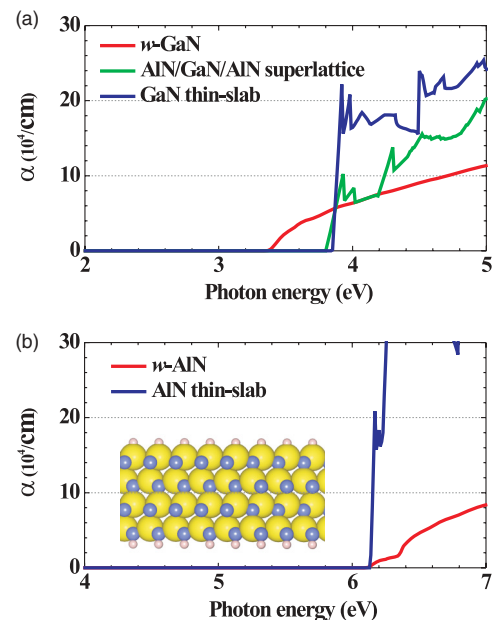


FIG. 4. (Color online) (a) The comparison of the calculated (average) absorption coefficient α between w -GaN, a 4-layer GaN thin slab, and the 20-layer-AIN/4-layer-GaN/20-layer-AIN superlattice. (b) The comparison of the calculated (average) absorption coefficient α between w -AIN and a 4-layer AIN thin slab.

“quantum” optical properties can be achieved. For example, from the Bohr effective mass model we can roughly estimate that the critical quantum thicknesses for AlN and GaN are around 1.8 and 3.1 nm, respectively. The calculated α of a 4-layer (~ 1 nm) GaN and AlN thin slabs are shown in Figs. 4(a) and 4(b). Obviously, a large enhanced absorption intensity can be realized in the GaN and AlN thin slabs. When the thickness of the thin slab is increased, the quantum size effect becomes weaker and the absorption or luminescence intensity at the absorption edge is decreased and close to that of bulk. For example, a 10-layer GaN thin slab with a thickness of ~ 3.5 nm exhibits an absorption spectrum similar to that of bulk GaN. More interestingly, our calculations indicate that the widely used superlattice structures (such as 20-layer-AlN/4-layer-GaN/20-layer-AlN)³ cannot achieve a large improvement in the absorption intensity of GaN compared to the thin slab we proposed, as shown in Fig. 4(a), mainly because the electron potential barrier induced by the AlN layers (~ 2 eV) is not high enough to realize a “real” 2D effect. Our understandings can also explain well the recent experimental observations that significant enhancements of absorption or luminescence intensity can be achieved in CdX

(X = Se, S, or Te) thin films only when their thicknesses are limited to a few layers.²⁴

IV. CONCLUSION

In conclusion, by combining first-principles calculations and experiments, we have addressed the question why *h*-BN could be a brighter emitter than AlN. The understanding of the unusual property in *h*-BN also suggests that the absorption or luminescence intensity at the fundamental absorption edge of an optical material can be greatly enhanced by confining its thickness into a few layers, which is more effective than the commonly used superlattice technology.

ACKNOWLEDGMENTS

This work was supported by the US Department of Energy under Contract No. DE-AC36-08GO28308 to NREL and under Contract No. FG02-09ER46552 to TTU. H.X.J. and J.Y.L. would like to acknowledge the support of Whitacre endowed chair positions through the ATT foundation. We would also like to acknowledge assistance from Qiang Xu of NREL and J. Li and S. Majety from TTU.

¹M. L. Cohen and J. R. Chelikowsky, *Electronic Structure and Optical Properties of Semiconductors* (Springer-Verlag, Berlin, 1988).

²P. Y. Yu and M. Cardona, *Fundamentals of Semiconductors: Physics and Materials Properties* (Springer-Verlag, Berlin, 2001).

³*Handbook of Luminescent Semiconductor Materials*, edited by L. Bergman and J. L. McHale (Taylor Francis Group, Boca Raton, FL, 2011).

⁴K. Watanabe, T. Taniguchi, and H. Kanda, *Nat. Mater.* **3**, 404 (2004); Y. Kubota, K. Watanabe, O. Tsuda, and T. Taniguchi, *Science* **317**, 932 (2007); K. Watanabe, T. Taniguchi, and H. Kanda, *Nat. Photon.* **3**, 591 (2009); R. Dahal, J. Li, S. Majety, B. N. Pantha, X. K. Cao, J. Y. Lin, and H. X. Jiang, *Appl. Phys. Lett.* **98**, 211110 (2011).

⁵G. Kresse and J. Furthmuller, *Comput. Mater. Sci.* **6**, 15 (1996).

⁶J. Heyd, G. E. Scuseria, and M. Ernzerhof, *J. Chem. Phys.* **118**, 8207 (2003).

⁷B. Huang, Q. Xu, and S.-H. Wei, *Phys. Rev. B* **84**, 155406 (2011).

⁸M. Gajdos, K. Hummer, G. Kresse, J. Furthmuller, and F. Bechstedt, *Phys. Rev. B* **73**, 045112 (2006).

⁹P. Giannozzi *et al.*, *J. Phys.: Condens. Matter* **21**, 395502 (2009).

¹⁰A. Marini, C. Hogan, M. Gruning, and D. Varsano, *Comput. Phys. Commun.* **180**, 1392 (2009).

¹¹*Properties of Group III Nitrides*, edited by J. H. Edgar (INSPEC, London, 1994).

¹²The irreducible representations are labeled according to the notations of G. F. Koster, J. O. Dimmock, R. G. Wheeler, and H. Statz, *Properties of the Thirty-two Point Groups* (MIT Press, Cambridge, MA, 1963).

¹³R. H. Parmenter, *Phys. Rev.* **100**, 573 (1955).

¹⁴G. D. Chen, M. Smith, J. Y. Lin, H. X. Jiang, S.-H. Wei, M. A. Khan, and C. J. Sun, *Appl. Phys. Lett.* **68**, 2784 (1996).

¹⁵J. Li, K. B. Nam, M. L. Nakarmi, J. Y. Lin, H. X. Jiang, P. Carrier, and S.-H. Wei, *Appl. Phys. Lett.* **83**, 5163 (2003).

¹⁶The spin-orbital coupling can mix Γ_6 and Γ_1 states. For simplicity of symmetry analysis, we assume here the spin-orbital splitting is much smaller than the crystal field splitting, which is true for AlN and BN.

¹⁷H. W. Streitwolf, *Phys. Status Solidi* **33**, 225 (1969).

¹⁸R. L. Benbow, *Phys. Rev. B* **22**, 3775 (1980).

¹⁹Y.-N. Xu and W. Y. Ching, *Phys. Rev. B* **44**, 7787 (1991); N. E. Christensen and I. Gorczyca, *ibid.* **50**, 4397 (1994); X. Blase, A. Rubio, S. G. Louie, and M. L. Cohen, *ibid.* **51**, 6868 (1995).

²⁰*Synthesis and Properties of Boron Nitride*, edited by J. J. Pouch and S. A. Alteroviz (Trans Tech, Switzerland, 1990).

²¹L. Song, L. Ci, H. Lu, P. B. Sorokin, C. Jin, J. Ni, A. G. Kvashnin, D. G. Kvashnin, J. Lou, B. I. Yakobson, and P. M. Ajayan, *Nano Lett.* **10**, 3209 (2010); Y. M. Shi, C. Hamsen, X. T. Jia, K. K. Kim, A. Reina, M. Hofmann, A. L. Hsu, K. Zhang, H. N. Li, Z. Y. Juang, M. S. Dresselhaus, L. J. Li, and J. Kong, *ibid.* **10**, 3209 (2010); K. K. Kim, A. Hsu, X. Jia, S. M. Kim, Y. Shi, M. Hofmann, D. Nezich, J. F. Rodriguez-Nieva, M. Dresselhaus, T. Palacios, and J. Kong, *ibid.* **12**, 161 (2012).

²²H. Zeng, C. Zhi, Z. Zhang, X. Wei, X. Wang, W. Guo, Y. Bando, and D. Golberg, *Nano Lett.* **10**, 5049 (2010).

²³B. Arnaud, S. Lebegue, P. Rabiller, and M. Alouani, *Phys. Rev. Lett.* **96**, 026402 (2006); L. Wirtz, A. Marini, M. Gruning, C. Attacalite, G. Kresse, and A. Rubio, *ibid.* **100**, 189701 (2008); L. Wirtz, A. Marini, and A. Rubio, *ibid.* **96**, 126104 (2006).

²⁴S. Ithurria, M. D. Tessier, B. Mahler, R. P. S. M. Lobo, B. Dubertret, and A. L. Efros, *Nat. Mater.* **10**, 936 (2011).